



# Estimation of Mechanical Properties of the Bakken Shales Through Convolutional Neural Networks

Chunxiao Li<sup>1</sup> · Dongmei Wang<sup>1</sup> · Lingyun Kong<sup>2</sup> · Mehdi Ostadhassan<sup>3</sup>

Received: 22 June 2021 / Accepted: 14 November 2021 / Published online: 16 January 2022  
© The Author(s), under exclusive licence to Springer-Verlag GmbH Austria, part of Springer Nature 2021

## Abstract

Effective mechanical properties of shale rocks can be determined by knowing the mechanical properties and distribution pattern of each comprising constituent. However, building the relationship between them is complicated and requires mathematical manipulations. In this study, by taking advantage of machine learning (ML) that is capable of delineating hidden patterns with the least sophistication, a new approach to estimate Young's modulus of shales by integrating deep learning convolutional neural networks (CNNs) into 2D elemental intensity distribution maps is presented. The generated SEM–EDX maps contain spatial distribution and intensity information of nine major elements abundant in a shale, Al, Ca, C, Fe, K, Mg, Na, S, and Si. The ground truth data are Young's modulus based on laboratory microindentation tests from ten samples. A total amount of 800 images were used for training and testing, and the trained CNNs were then used to predict Young's modulus of shale samples by feeding the elemental images. The predicted Young's modulus exhibited an acceptable relative error of 6.5% and in a much faster time and less effort compared to the laboratory tests. Ultimately, we believe that this novel method has great potential for field applications due to simplified requirements for sample preparation and laboratory apparatus.

## Highlights

- A deep learning Convolutional Neural Networks model was employed on 2D elemental intensity distribution maps to predict the mechanical properties of shales from the Bakken Formation.
- Easy-obtained EDS maps were used as input and Young's modulus obtained from laboratory microindentation tests was used as output to train the CNNs model.
- The trained model exhibited good performance on predicting the Young's modulus of unseen samples, with an average relative error of 6.5%.

**Keywords** Mechanical properties · Bakken shale · EDS mapping · Machine learning · Convolutional neural networks · Microindentation

## 1 Introduction

Successful production of hydrocarbon from unconventional shale plays relies heavily on our knowledge of mechanical properties of the formation including elastic moduli and strength (Dahi-Taleghani et al. 2011; Hoek and Martin 2014). Generally, shales are extremely heterogeneous composite materials, with various constituents and complex microstructure. As a consequence, researchers face many challenges to study their mechanical properties (Li et al. 2018a, b, 2019a). Conventional laboratory mechanical testing, such as uniaxial and triaxial compressive strength testing, is time-consuming and expensive. Additionally, the

✉ Chunxiao Li  
chunxiao.li@und.edu

<sup>1</sup> Harold Hamm School of Geology and Geological Engineering, University of North Dakota, Grand Forks, ND, USA

<sup>2</sup> Department of Petroleum Engineering, University of North Dakota, Grand Forks, ND, USA

<sup>3</sup> Institute of Unconventional Oil and Gas, Northeast Petroleum University, Daqing, China

acquisition of rock samples of good quality for these laboratory measurements can become challenging and sometimes impossible due to the brittleness of the samples and their availability, as well. Thus, numerical modeling methods that are based on micromechanical theory are well established in many studies (Goodarzi et al. 2017, 2016; Li et al. 2019a, b; Liu et al. 2018; Zhao et al. 2019). However, these studies are generally carried out on assumptions in the model where interactions between various components are simplified (Goodarzi et al. 2017, 2016; Zhao et al. 2019).

Recently, indentation techniques that show great promise as an approach in assessing the mechanical properties of shales at a local scale have gained popularity compared to the conventional macroscale methods. Instrument indentation is a technique that allows us to measure the mechanical properties of porous composite comprised of multiple minerals. This technique involves a small probe that penetrates into a flat surface of the sample, while the applied force and displacement of the probe are then recorded concurrently to calculate the mechanical properties, including Young's modulus and hardness (Ulm and Abousleiman 2006). The mechanical properties of shales are scale-dependent (Abedi et al. 2016b; Li et al. 2021a; Veytskin et al. 2017). At a macroscale, the mechanical properties of shale are measured in the lab on core plugs or bulk samples which contain natural fractures and weak bedding planes. In comparison, the indentation technique can be used to investigate the mechanical properties at a fine scale by avoiding from the effect of uneven distributed microfractures. Many existing analytical models usually ignore these features by considering shales as composite materials with different minerals and organics geometrically stacked together. Therefore, the mechanical response is determined by microstructures, components configuration, and grain-to-grain interactions (Sayers 2013; Goodarzi et al. 2016, 2017; Zhao et al. 2019).

Considering the sophisticated relationships between various components in shales, artificial intelligence (AI) and machine learning (ML) techniques have enabled us to tackle these problems more feasibly. Machine learning techniques are generally utilized to uncover the inherent rules and to highlight hidden features. In the past few years, a large number of studies using ML methods have been conducted to solve problems in the fields of petroleum engineering and geosciences (Izadi et al. 2015; Khan et al. 2018; Li et al. 2019a, b, c, 2021b; Misra et al. 2019; Torlov et al. 2017). Among various machine learning algorithms and their applications, artificial neural network (ANNs) has demonstrated outstanding performance on various tasks. The typical ANNs are comprised of multiple layers, including an input layer, hidden layers, and an output layer, and each layer contains a various number of nodes (Hassoun et al. 1995). The calculation is passed through by the connected nodes at each layer, while the connections carry weights, bias, and non-linear

transformations. The outputs are then sent to the next layer of the network (Hassoun et al. 1995). The ANNs models should be trained based on a large amount of dataset, while during the training process, the values of the weights and biases by minimizing the error via backpropagation algorithms are iteratively updated. Moreover, ANNs with multiple hidden layers are classified under deep learning models. In this regard, convolutional neural networks (CNNs) is a category of deep neural networks, which has presented the state-of-the-art performance in computer vision applications. CNNs generally follows a similar basic structure as ANNs, with special convolutional and pooling layers (Simard et al. 2003). Though, unlike ANNs, where all nodes are fully connected to one other, convolutional layers utilize filters over multiple image locations and preserve the spatial relationships. Also, pooling layers are used to simplify the output information from the previous convolutional layer (Krizhevsky et al. 2012). Compared to classical machine learning algorithms that mostly rely on hand-engineered filters/algorithms to extract specific features, ANNs/CNNs automatically learn the complex hidden features and therefore can exhibit outstanding performance when dealing with complex data, such as images (Sultana et al. 2018).

Studies using image-based deep learning methods to estimate mechanical properties are limited. The majority of machine learning methods in determining the geomechanical properties of rocks so far are limited to well logs. For example, He et al. (2018) reported a comparative study of using shallow learning models to calculate compressional and shear wave travel-time logs (He et al. 2018). Gupta et al. (2019) compared the performance of several machine learning regressors in the generation of synthetic sonic logs and the prediction of mechanical properties (Gupta et al. 2019). The application of machine learning in imagery to determine mechanical properties is relatively limited. Li et al. (2019c) employed CNNs to establish a relationship between simplified mineralogy maps and effective mechanical properties of shale rocks. The labeled mechanical behavior of each sample was obtained using a finite-element model with generated input (Li et al. 2019c). However, obtaining the mineralogy maps of rocks is time-consuming, which either needs special proprietary software or needs to be done by experienced technicians on (back scatter electron) BSE-SEM and EDX (energy-dispersive X-ray) images. In contrast, the EDS(X) images are easily obtained. Elemental mapping involves rastering an electron beam, point by point over an area of interest on a sample surface, and at the same time, the spatial distribution and intensities of each element are mapped as pixel-by-pixel (bitmap) images. In geosciences, surface distribution and intensity information of the elements in a 2D map over the same area allow the users to determine the presence of mineral phases. Additionally, microstructural information of shale rocks such as the shape of mineral particle distribution pattern

and interaction between mineral phases can be obtained in these electron micrographs.

In this study, a new approach to estimate Young's modulus of shales by integrating deep learning CNNs into 2D elemental intensity distribution maps is presented. An end-to-end CNNs model was employed to link the comprising chemical elements of shale samples with corresponding mechanical properties of the same area. To do so, A CNNs model was trained with the elemental maps as input and Young's modulus as ground truth data. In comparison to 2D mineral maps, elemental images are much easier to generate, since they are the main result obtained from electron microscopy. Hence, we can skip generating mineral maps as a connecting bridge to estimating the mechanical properties, which is the most labor-intensive and time-consuming step. The labeled data were obtained from laboratory measurements of Young's modulus via laboratory microindentation tests. Next, the CNNs model was trained and further utilized for the mechanical behavior prediction of the samples. This study shows that collecting quick and easy elemental maps from the surface with SEM–EDS would be sufficient to estimate the mechanical properties of the samples.

## 2 Materials

Samples used in this study were retrieved from the Bakken Formation, Williston Basin, North Dakota, U.S. The Williston Basin is a major energy resource that covers western North Dakota, the northeastern region of Montana, and extends into parts of Canada (Fig. 1a). The Bakken Formation is the most significant hydrocarbon-bearing layer within the basin. It comprises three distinct members, the Upper, Middle, and the Lower Bakken. The upper and lower

members are mostly black, organic-rich shales, with an average total organic carbon (TOC) content of 8 wt% and the middle member is fine carbonate-rich sandstone and siltstone (Abarghani et al. 2018). Ten shale samples taken from the lower and upper members from three different wells were used in this study (Fig. 1b). The samples were purposely chosen from various locations to reflect variations in mineralogy, thermal maturity, and microstructures.

## 3 Methodology

Methods to collect the input data, element intensity maps, and labeled data, Young's modulus, are provided in this section, followed by a description of the architecture of CNNs model, and a flowchart to summarize the entire workflow.

### 3.1 Acquisition of Input Dataset–Elemental Density Images

The input data are element density maps. An element density map is an image showing the spatial distribution and intensity of the element on the surface of the sample (Wenner et al. 2017). Acquisition of elemental density images was carried out by energy-dispersive X-ray spectroscopy (EDS/EDX). An FEI Quanta FEG 650 SEM instrument, equipped with an X-ray detector, was used to acquire the map of the elements on the area of investigation. The operation principle is based on the ejection of electrons from shells near the atom of an element, and it leaves behind a hole in the inner shell. The generation of X-ray involves energy releasing when electrons jumping from the outer higher energy shell to the inner lower one to fill the hole. The energy and the amount of the emitted X-rays can be detected by an

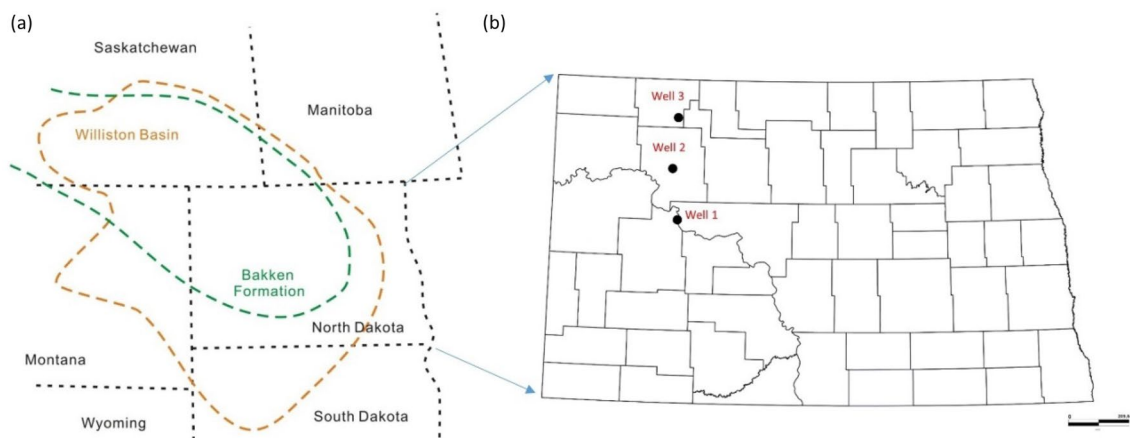


**Fig. 1** **a** Schematic maps showing the location of the Bakken Formation in Williston Basin. The Bakken Formation covers western of North Dakota, US, northeastern region of Montana, US, and extended

to Canada; **b** Well locations where samples are retrieved, shown on the zoomed map of North Dakota

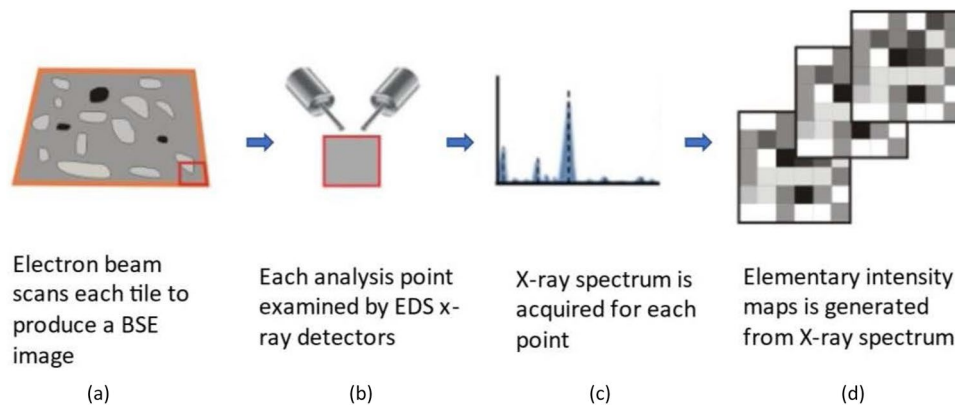


**Fig. 2** Schematic illustration of element density mapping through Energy-Dispersive X-ray spectroscopy. Acquiring the element intensity maps requires the following steps: **a** scanning a Back-scattered electron (BSE) image via SEM, and the image was then divided into

multiple tile; **b** for each point within a tile, the X-ray detector was used to get **c** the X-ray spectrum, which contains the intensity information for elements, and after all the points were examined and analyzed, **d** a spatial intensity map was generated for each element

energy-dispersive spectrometer. Since the wavelength of the X-rays is unique to each element, it can be used as a characteristic of the atomic structure of the emitting element (Shindo and Oikawa 2002). The overall maps constitute of existing elements on the surface with their proportion at the submicron scale (Saif et al. 2017).

Mapping of the element intensity is based on compiling specific elemental composition across the certain area of the sample, following these steps (Fig. 2): (a) electron beam scans the target area to produce a BSE image, (b) EDS X-ray detector examines each pixel by desired resolution to collect an X-ray spectrum at each grid block, and extracts information about what elements are present and the proportion of each one, and (c) an energy window is defined for each element of interest and the number of X-rays detected in the energy window of the element at each X, Y location is plotted, thus the intensity maps are then created. These maps illustrate regions of relatively high and low elemental intensity (Shindo and Oikawa 2002).

### 3.2 Acquisition of Labeled Data (Young's Modulus) via Microindentation

The labeled data are Young's modulus measured through laboratory microindentation tests. The instrumental indentation is a load- and- displacement sensing technique, which has been broadly used in characterizing mechanical properties of a variety of materials at a microscale or nanoscale (Abedi et al. 2016a, b; Bobko and Ulm 2008; Bobko 2008; Fischer-Cripps 2011). The indentation procedure involves pressing an indenter with a fine probe on the sample surface by applying a load. During this process, the applied load  $P$  and displacement  $h$  are recorded by sensors. The elastic properties of the materials are estimated from the measured

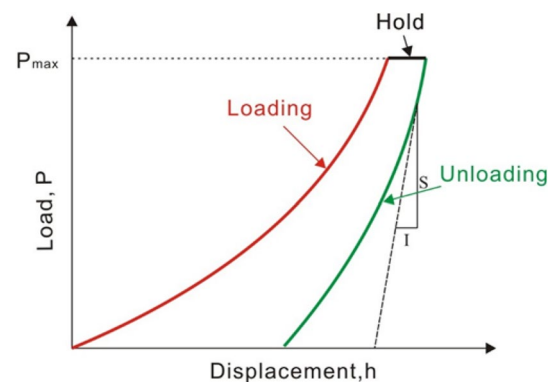


**Fig. 3** Load–displacement curve of indentation (modified from Hu and Li 2015). There are three sections in each indentation procedure. It involves pressing a fine probe into the surface of the shale sample by applying a load (Loading section, as shown in red). When the applied load matches the predefined maximum load,  $P_{max}$ , the probe keeps the load and holding for a period of time (Holding section, 200 s in this study, as shown in black), and then, the probe lifts from the sample surface to the original position (Unloading section, as shown in green). The Young's modulus for each indent was then calculated using information obtained from the unloading curve by Eqs. 1–4

indentation load–displacement curve (Fig. 3) via the following analytical model (Oliver and Pharr 1992, 2004):

$$E_r = \frac{\sqrt{\pi}}{2} \frac{S}{\sqrt{A_c}} \quad (1)$$

$$H = \frac{P}{A_c} \quad (2)$$

$$S = \left( \frac{dP}{dh} \right)_{h=h_{max}} \quad (3)$$

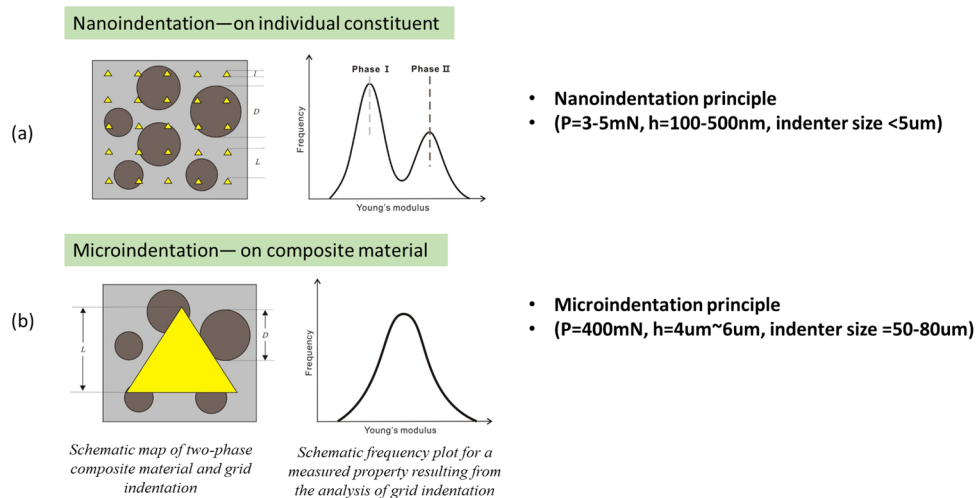


**Fig. 4** Comparison between principles of **a** nanoindentation and **b** microindentation.  $l$  denotes the indenter size,  $D$  is the characteristic size, and  $L$  is the spacing distance of indenters. The circle in dark brown illustrates the mineral particles, and the gray represents the matrix for a two-component material. The yellow triangle shows the indenter. For shale samples, when a relative smaller load (with  $P_{\max}=3\text{--}5\text{ mN}$ ) is applied, the displacement of the probe and the

indenter size is relative small, and the obtained Young's modulus can be used to reflect the mechanical properties of each comprising mineral as shown in **(a)**; In contrast, in microindentation with larger load (with  $P_{\max}=\sim 400\text{ mN}$ ), a larger indenter would be generated and it then reflects the average mechanical response of the composite material

Here,  $E_r$  is the reduced Young's modulus, which is a function of the stiffness,  $S$ , and the indent contact area,  $A_c$ . Stiffness,  $S$ , is calculated by fitting the slope of the upper portion of the unloading curve (Fig. 3). Additionally, Hardness,  $H$ , can also be estimated by the peak load,  $P$ , and the contact area,  $A_c$ . The Young's modulus can then be calculated by the following equation (Constantinides et al. 2006; Hertz 1881):

$$\frac{1}{E_r} = \frac{1-\nu_s^2}{E_s} + \frac{1-\nu_{\text{tip}}^2}{E_{\text{tip}}} \quad (4)$$

Here,  $\nu_s$  and  $\nu_{\text{tip}}$  denotes the Poisson's ratio of the sample and the probe, respectively, and  $E_s$  and  $E_{\text{tip}}$  are Young's modulus of the sample and the probe, correspondingly. It has been proved that the value of Poisson's ratio does not significantly affect the ultimate Young's modulus that is derived, therefore, as an accepted value; 0.3 is considered for further calculations (Liu et al. 2018).

It is important to note that the mechanical property values obtained could either reflect the average property of the sample (mesoscopic) or the response of a single mineral (microscopic), depending on the magnitude of the applied load and size of the indenter. This being said, delineating the governing relationship between microstructures (minerals/organics and pore space) and mechanical properties would be critical to obtaining meaningful outcomes and properly interpreting the results. The loading force during the microindentation experiments must be chosen in accordance with the material (here shale) heterogeneity and constituent components to

provide us with the average and correct mechanical response of the sample (Ulm and Abousleiman 2006). Considering a heterogeneous material comprised of two distinguished phases, when the indent size ( $l$ ) is smaller than the characteristic size ( $D$ ) of the particles, the mechanical response from each indent would be the properties of an individual phase, and the density distribution curve of the overall obtained Young's modulus from the entire dataset should display two different peaks as a bimodal curve (Fig. 4a). In contrast, to access the bulk properties, or the average mechanical response of the composite material, a much higher load force should be chosen, so that the indent size can be much larger than the characteristic size ( $D$ ),  $l > D$ . In this way, we can ensure that each indentation will assess the average property of the heterogeneous shale sample (Fig. 4b). Previous studies have shown that at least  $4\ \mu\text{m}$  displacement of each indents can be used for examining the bulk mechanical properties of shale samples (Zhao et al. 2019). In this study, experimental indentation tests on the Bakken shale samples demonstrate that a maximum load of  $400\text{ mN}$  can generate indents large enough, while other necessary conditions are followed ( $P_{\max}=400\text{ mN}$ ).

The indentation tests were performed using a Berkovich pyramidal tip with TI 980 Triboindenter, Hysitron, Minneapolis, Minnesota). Each sample was indented 50 times with two sets of  $5 \times 5$  grid patterns. The indenter locations were randomly selected within each sample. A load control model with a maximum load of  $400\text{ mN}$  was used. A constant hold time was needed to decrease viscoelastic effects

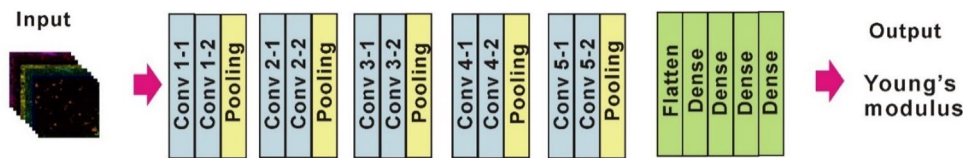


**Fig. 5** Architecture of the modified CNNs model. The original VGG-16 model has two convolution layers for the first two Conv. Blocks, and has three convolution layers for the Conv. Block 3–5, and three

Dense layers attached in the end. In our modified model, we use two convolution layers for all the Conv.Blocks, and increase one more Dense layer.

while measuring Young's modulus. Since the examined samples in this study are organic-rich, a relatively long constant holding time, 200 s, was chosen following the loading stage. The indenter was advanced at a rate of 40 mN/s to 400 mN, held at a constant hold for 200 s, and unloaded at a rate of 40 mN/s, and then, the elastic modulus calculated from each curve for each sample was obtained by averaging the dataset.

### 3.3 Convolutional Neural Networks' Architecture

A standard CNNs architecture consists of several convolutional blocks, and each convolutional block typically is comprised of one or several convolutional layers, followed by pooling layers, and non-linear activation transformation (Sultana et al. 2018). A fully connected layer is attached at the end of the architecture, as shown in Fig. 5:

- Convolutional layer: the convolution layer takes an image as input and applies transformations by filters. The spatial relationship of the input images is passed into the filtered maps, and also referred to as feature maps. The training process uses gradual modification to reduce any loss learnings from the parameters of the filtered images. The parameters of the filters are shared across the input space, which reduces the number of trainable parameters compared to the fully connected layers.
- Pooling layer: a pooling layer is usually designed to attach the convolutional layers in CNNs to simplify the feature maps and reduce the number of model parameters, as well. The maximum pooling is the most popular pooling layer, which applies a maximum function to a receptive field (usually a  $n \times n$  kernel).
- Non-linear activation transformation: similar to the ANNs, non-linear transformation carried out by the activation function is included in the CNNs' architecture. The non-linearity of rectified linear unit (ReLU) defined as  $ReLU(x) = \max(x, 0)$  presents advantages in preventing vanishing gradient problems (Goodfellow et al. 2016). Conventionally, the ReLU term is used in deep CNNs models.
- Fully connected layer: Fully connected layers are added to the last convolutional layer. The function of this layer

is to transform all previous extracted scalarized features to a final class score for classification tasks or to some values for regression tasks.

A number of classic CNNs architectures have been proposed and shown outstanding performance on image recognition and objective detection. These architectures also have proven successful applications on different problems. Classic architectures including AlexNet (Krizhevsky et al. 2012), ResNet50 (He et al. 2016), VGG (Simonyan and Zisserman 2015), and GoogLeNet (Szegedy et al. 2015) have exhibited excellent performance in image classification. In this study, the VGG-16 architecture was chosen as the basic model and further modified. The reason to choose the VGG model is the small receptive field of  $3 \times 3$  that is used in its architecture. This would be suitable in capturing the details of the contact interaction of grain particles in the element maps. The original architecture of the VGG-16 model consists of five convolutional blocks, each block comprising of two or three convolution layers followed by one pooling layer, and three full-connected dense layers attached in the end. In the original VGG-16 model, the initial input has the size of  $224 \times 224 \times 3$ .

In this study, the following modifications were made for the architecture of the model, as shown in Fig. 5: we keep the structure of five convolutional blocks, and each block has two convolutional layers and one pooling layer, compared to the variable number of convolutional layers in the original VGG-16 model. Then, in the final block, we increase the number of dense layers to four, compared to the original model which has three dense layers. For each convolutional layer, the filter size is  $3 \times 3$ , the padding size is 1, and the stride size is  $2 \times 2$ . ReLU activation transformation was used. Additionally, the input data dimension was modified from originally  $224 \times 224 \times 3$  to  $112 \times 112 \times 9$ , where  $112 \times 112$  represents the size of each element maps, and 9 represents that there are 9 element intensity channels. The number of learnable parameters in this CNNs' model is around 12 million (Table 1), which is around only 9% of that of the original VGG-16 (Simonyan and Zisserman 2015). For more details regarding the model architecture, training process and prediction, a Github repository link: <https://github.com/>

**Table 1** Architecture and number of parameters in the CNNs model

Layer	Output size			Number of parameters
	W	H	C	
Input	112	112	9	0
block1_conv1	112	112	32	2624
block1_conv2	112	112	32	9248
block1_pool	56	56	32	0
block2_conv1	56	56	64	18,496
block2_conv2	56	56	64	36,928
block2_pool	28	28	64	0
block3_conv1	28	28	128	73,856
block3_conv2	28	28	128	147,584
block3_pool	14	14	128	0
block4_conv1	14	14	256	295,168
block4_conv2	14	14	256	590,080
block4_pool	7	7	256	0
block5_conv1	7	7	256	590,080
block5_conv2	7	7	256	590,080
block5_pool	3	3	256	0
flatten	2304			0
fc1	4096			9,441,280
fc2	100			409,700
fc3	100			10,100
fc4	100			10,100
Prediction	1			101
Total				12,225,425

[chunxiaoqiuyue/Estimate\\_Young-s-modulus-from-EDS-maps](#) is provided for reference.

### 3.4 Overview of the Computational Framework

The purpose of the computational framework is to train a valid CNNs model, which can effectively predict mechanical properties via input elements' intensity images. There are four steps in the proposed computational framework: (a) building the input database by collecting the elements density maps through the EDS experiments, (b) collecting mechanical properties, Young's modulus, of samples through indentation experiments, (c) building a CNNs model and training the model using input images and mechanical properties dataset, and (d) predicting the mechanical properties using the trained CNNs model (Fig. 6).

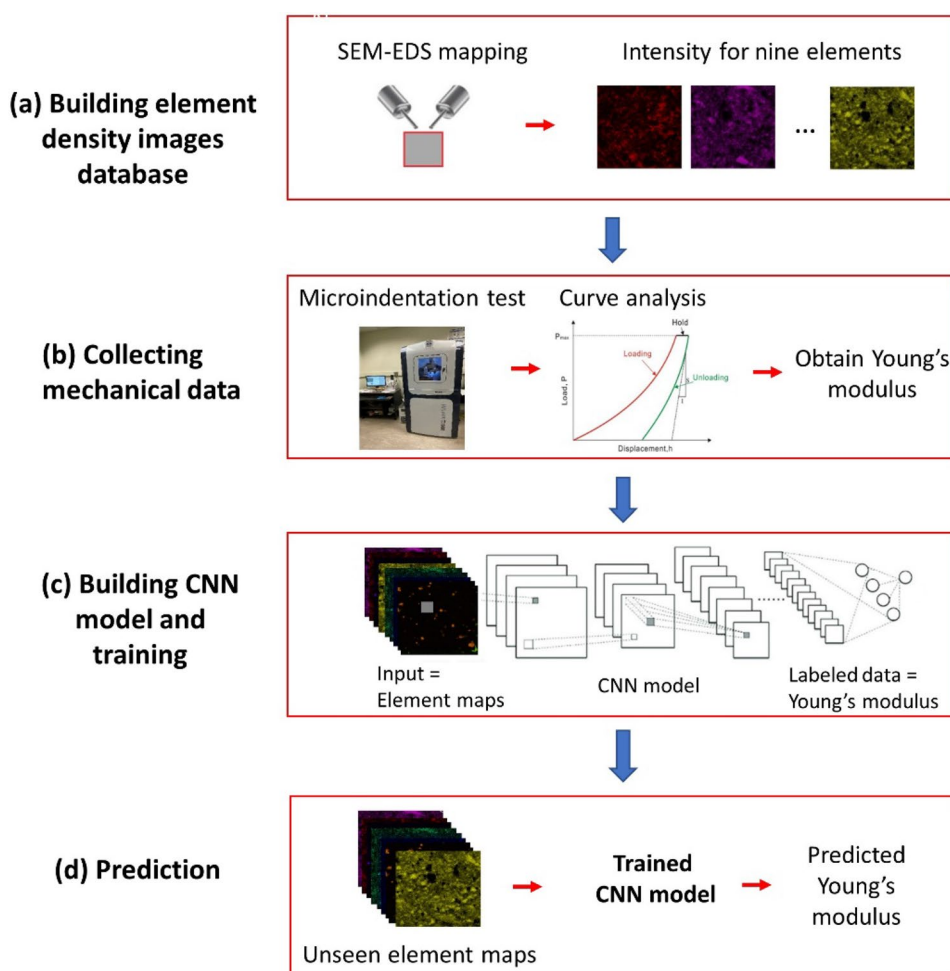
## 4 Results and Discussion

### 4.1 Elements Density Images

Intensity distribution maps of nine most common elements within shale rocks, including aluminum (Al), calcium (Ca), carbon (C), iron (Fe), potassium (K), magnesium (Mg), sodium (Na), sulfur(S), and silicon (Si), were generated (Fig. 7). Twenty different locations were scanned for each shale sample. The original map of each scan area was specified by  $768 \times 1024$  pixel size, with a pixel resolution of  $0.25\mu\text{m}/\text{pixel}$ , which cultivated an area of  $192 \times 256 \mu\text{m}$  for each scanned area. The smallest area over which a measurement can be made that will yield a value representative of the whole sample is referred to as a representative element area (REA). REA studies of 2D mineral maps of the Bakken shales have confirmed that the fractions of each mineral calculated from the box-counting method would not vary much when the boxing size becomes larger than  $100 \mu\text{m}$  (Liu et al. 2018). Furthermore, a similar study of the REA in the Bakken shale via SEM maps in terms of porosity has reported that the REA can be a few hundreds of micrometers (Saraji and Piri 2015). In this study, by considering the REA and collecting adequate images to train our model, we chose an area of  $125 \times 125 \mu\text{m}$  as the size of the basic REA images. Besides, since CNNs models use a matrix of  $n \times n$ , for each scanned area, an image with a size of  $125 \mu\text{m} \times 125 \mu\text{m}$  was randomly cropped. A data augmentation technique was adopted next for generating a good number of training images, which resulted in the total number of 800 sets of elements density images (10 samples  $\times$  20 scan locations per sample  $\times$  4 randomly cropped sub-image per scan location) in the entire image dataset.

Additionally, the brightness of a given pixel in the 2D map represents the relative intensity of the corresponding element. It was found that *Si* was the most widely spread in the samples, followed by *Al*, *K*, and *Ca*, while *Ca*, *Mg*, *Na*, *S*, and *Fe* are less abundant. The correlation matrix of nine channels/elements densities demonstrated the relationship among densities of different elements, where 1 indicates a perfect positive linear correlation between two variables, and  $-1$  indicates a perfect negative linear correlation, while 0 means no linear correlation between two variables (Fig. 8). In our study, three sets of clearly positive correlations were noted, as shown in gray–black, and black in the correlation matrix. The existence of *Al* vs. *K*, *Mg* vs. *Ca*, and *S* vs. *Fe* is highly positively related, since these elements are co-existing in most minerals. Chemically, each mineral has a fixed elemental composition. For example, *K*-feldspar has the formula of  $KAlSi_3O_8$ , and therefore, the presence of *Al* is strongly related to the presence of *K*. In contrast, a strong negative correlation between elements was observed as only

**Fig. 6** A general overview of the proposed framework: **a** collecting intensity maps of nine elements via SEM–EDS mapping; **b** collecting Young’s modulus by laboratory microindentation tests; **c** building CNNs model and training with element maps as input data and Young’s modulus as labeled data; **d** using trained model to predict Young’s modulus value for unseen samples.



one mineral can be present at each pixel. For elements that do not exist within the same mineral, a negative correlation, such as Si vs. C, Si vs. Ca, Si, vs. Fe, and Si vs. S was observed.

With chemical information of the minerals, not only raw elemental composition and distribution information can be obtained, but mineral phases can be mapped with additional processing of the EDS maps. For example, the high intensity of *Ca* and *Mg* indicates the existence of dolomite and the locations of the relatively high intensity of *Fe* and *S* refers to the existence of pyrite. Previous studies have already reported mineral classification and segmentation using the EDS maps (Knaup et al. 2019; Li et al. 2021b; Tang and Spikes 2017). This process is commonly done by proprietary software, though, in this study, we used the end-to-end method where the EDS maps were fed into the learning models directly, instead of using the developed mineral maps or other features to predict mechanical properties.

## 4.2 Mechanical Dataset

Indentations were conducted on the shale samples, and each sample was specified with two sets of  $5 \times 5$  grid indents, with a total of 50 indents on each sample. For each indent, Young’s modulus was calculated from the load–displacement curves (Fig. 3). Figure 9 illustrates the load–displacement curves of Sample 4 as a representative. It explains that with the same maximum load setting, the displacements for Sample 4 vary due to the heterogeneity in shale samples and the displacement for most curves is in the range of 4–5  $\mu\text{m}$  at the maximum load of 400 mN.

Based on the analysis of the load–displacement curves, the reduced Young’s modulus is calculated from Eq. (1) through Eq. (4). Due to the highly heterogeneous nature of shales, the calculated Young’s modulus displayed variations among indented points within the same sample (Figs. 9, 10). An arithmetically averaged value of Young’s modulus was calculated and used as the ground truth label for each sample. The values of Young’s modulus are obtained in a range from 15.20 to 20.39 GPa among the samples, with Sample 4 exhibiting the highest value, and Sample 5 the lowest.

**Fig. 7** Maps of the element density of cropped sub-images for element Al, C, Ca, Si, K, Mg, Na, S, and Fe. Each image has the size of  $125\ \mu\text{m} \times 125\ \mu\text{m}$  and the brightness indicates the intensity of each element.

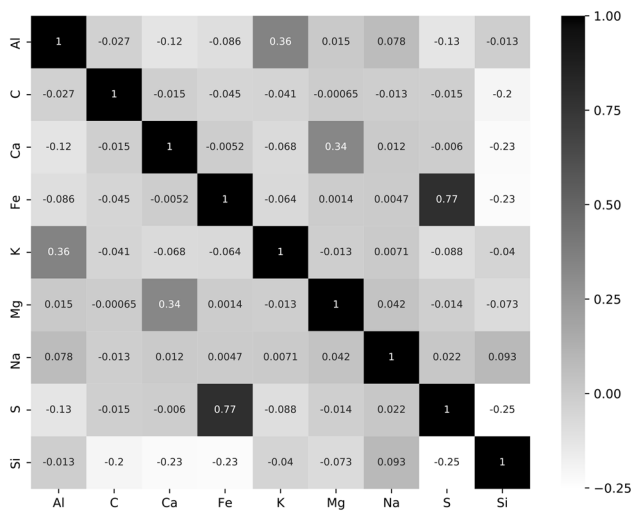
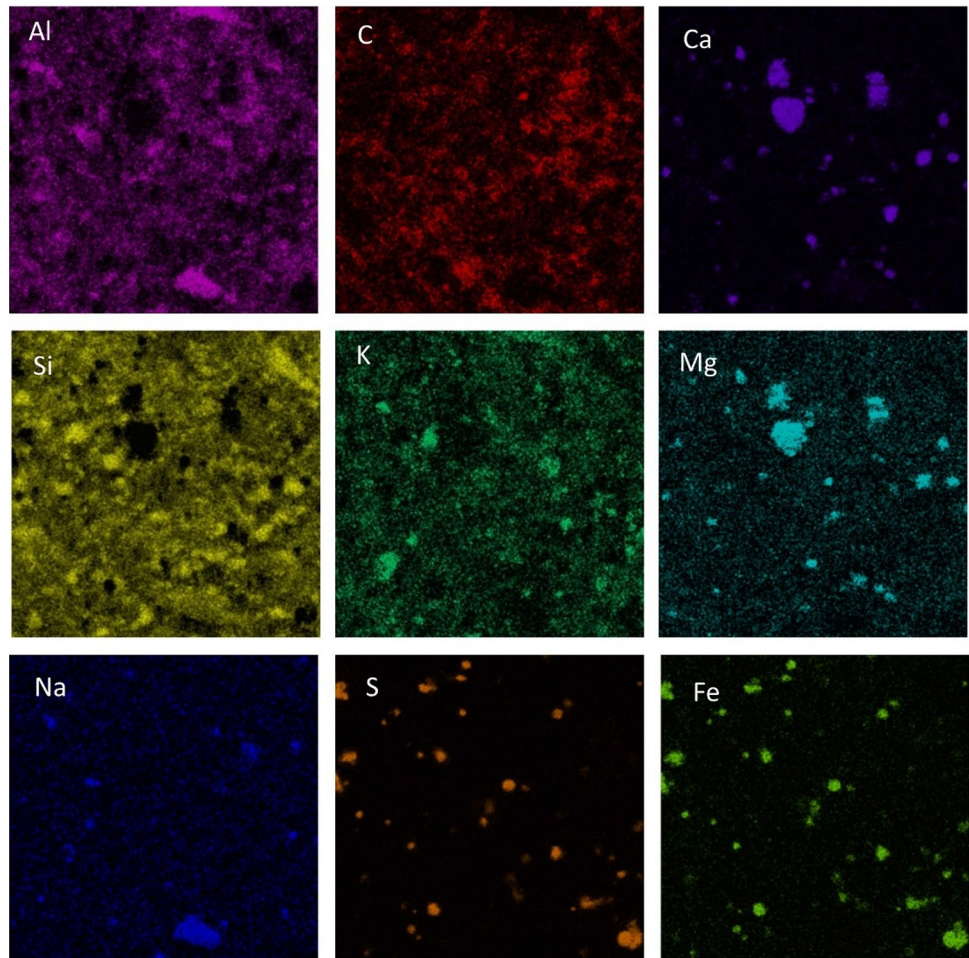


**Fig. 8** Correlation matrix among elemental intensity. Zero denotes no linear correlation; 1 and -1 each indicates perfect positive and negative linear correlations, respectively. Al vs. K, Mg vs. Ca, and S vs. Fe are highly positively related, since these elements are co-existing in minerals abundant in shales.

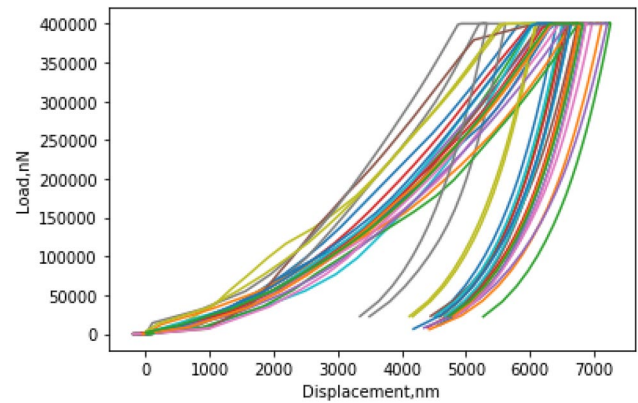


**Fig. 9** Load–displacement curves from indentations of Sample 4. At the maximum load of 400 mN, the displacement of most curves is in the range of 4–5  $\mu\text{m}$

### 4.3 Training Process

The entire dataset was divided into training and testing, where the testing dataset made 25% of the overall dataset. All weights and biases of CNNs model were updated using

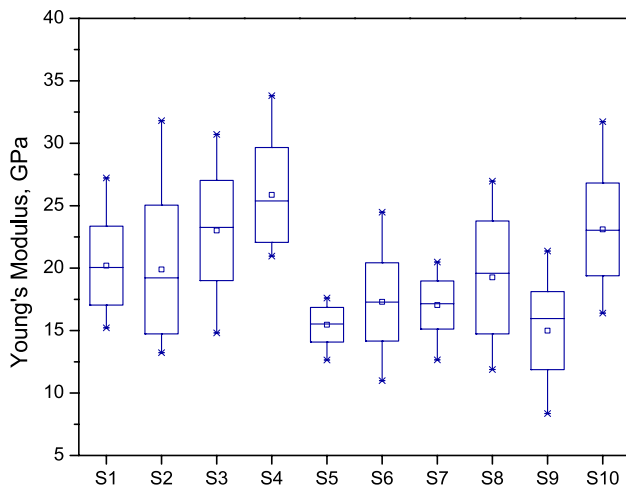


**Fig. 10** Box chart of Young's modulus obtained from indentation experiment (S on the  $x$ -axis, refers to sample numbers), Sample 4 exhibiting the highest value, and Sample 5 the lowest.

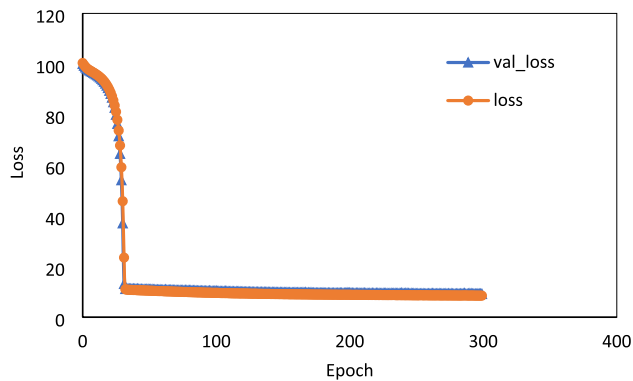
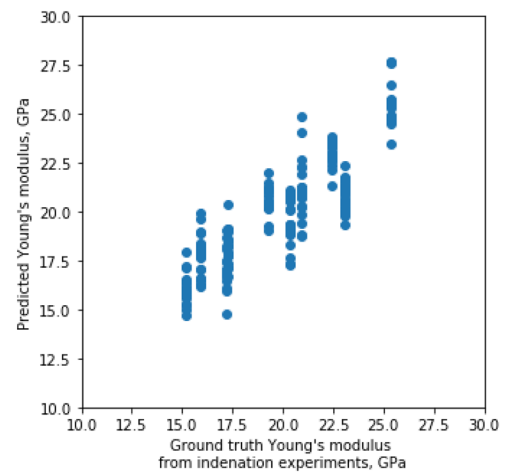


**Fig. 11** Loss decreasing during training process. The loss for training dataset is in orange, while that for validation in blue. Total 300 epochs with a batch size of 16 and learning rate of  $1e^{-7}$  were used. The loss changes smoothly at the beginning and then has a sharp decrease, and after 30 epochs, it reaches a plateau.

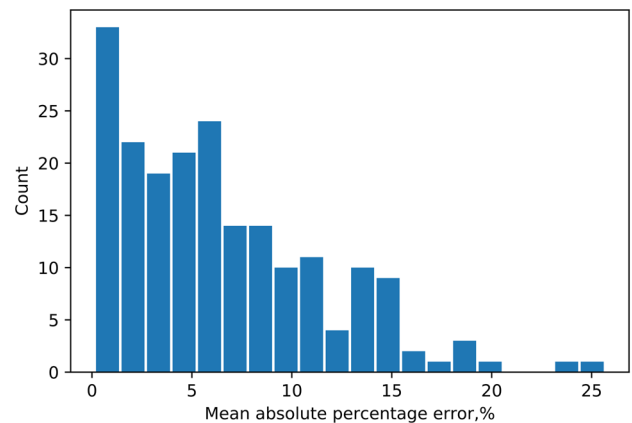
stochastic gradient descent (SGD) with a mini-batch size of 16 to avoid high-cost local minima. A learning rate of  $1e^{-7}$  is used in this optimizer. The objective function is the mean absolute percentage error (MAPE), which can be expressed in the following equation:

$$M = \frac{1}{n} \sum_{t=1}^n \left| \frac{A_t - F_t}{A_t} \right|, \quad (5)$$

where  $A_t$  is the ground truth, the value of Young's modulus, and  $F_t$  is the predicted Young's moduli. During the training process, 300 epochs were conducted. The training loss at the initial iteration steps was significant due to the randomly assigned weights and biases. Though, the training loss then



(a)



(b)

**Fig. 12** **a** Predicted results of Young's modulus compared with the laboratory data; the  $x$ -axis shows the ground truth data obtained from laboratory microindentation, while the  $y$ -axis shows the predicted Young's modulus from the trained model. **b** Histogram of mean absolute percentage error for the test dataset, showing that most of the test data have the error smaller than 15%, with an averaged error of 6.5%

descends dramatically after several iterations are completed (Fig. 11).

#### 4.4 Predicting the Moduli of Unseen Samples

The trained network for Young's modulus of unseen EDS image prediction was performed in the final step. Figure 12a displays the predicted results: the  $x$ -axis is the labeled/true value of the testing samples, while the  $y$ -axis represents the predicted Young's modulus value. This figure indicates that the predicted Young's modulus values are in good agreement with the data measured from the laboratory tests. Additionally, for each sample, the predicted Young's modulus value exhibited variations due to the highly heterogeneous nature of the samples. Histograms of MAPE among all samples demonstrated that for most of the test data points, errors

between the prediction and ground truth are less than 10%, with an average error value calculated as 6.5%, which is within an acceptable range compared to the results obtained from the laboratory tests with higher error percentage (Fig. 12b).

### 4.5 Discussion of Advantages and Limitations

It is worth understanding why the proposed method provides good predictive performance. A critical prerequisite of satisfactory predictive performance is that Young’s modulus of rocks is indeed a non-linear function of the information that can be extracted from the EDS maps, mostly the mineral information. It is well known that the effective material properties of shale rocks are determined by the mechanical property and distribution pattern of each forming constituent and their configuration. In the analytical method for estimating the mechanical properties, based on the micromechanical theorem, this can be described as follows (Mori and Tanaka 1973):

$$C_{hom} = \sum_{r=1}^N f_r C_r : \left[ \mathbb{I} + \mathbb{P}_{I_r}^0 : (C_r - C_0) \right]^{-1} \times \left[ \sum_{s=0}^N f_s : \left[ \mathbb{I} + \mathbb{P}_{I_s}^0 : (C_s - C_0) \right]^{-1} \right]^{-1}, \tag{6}$$

where  $C_0$  and  $C_r$  (or  $C_s$ ) are the stiffness tensor of the matrix phase and inclusion phase; representatively,  $f_r$  or  $f_s$  denotes the proportion of each phase;  $N$  is the total number of phases.  $\mathbb{P}_{I_r}^0$  or  $\mathbb{P}_{I_s}^0$  are tensors related to the shape and distribution patterns of the comprising composition (Laws 1977). Based on the equation, it is shown that the mechanical properties are a non-linear function of the fraction, mechanical properties, and the contact boundaries of mineral phases. As described earlier, through elemental mapping, the mineral phases, their fractions, spatial distribution, and their configuration can be extracted through these elemental maps. The convolutional transform in the CNNs model can capture and establish the connection between these features and the mechanical properties. Additionally, during the iterations when optimization is in process, the CNNs can identify the useful information, and filter out irrelevant features.

However, there are some limitations on this proposed method. First, as mentioned previously, the mechanical properties of shales are scale-dependent. The proposed approach is based on a mesoscopic point of view. For both the element density maps and the Young’s modulus measured from microindentation tests, the effect of nature fractures and weak bedding planes for the mechanical properties are not considered. Therefore, the Young’s modulus mentioned in this study might have some difference between values measured from traditional mechanical tests. Second, even we

have as many of 50 indents on each shale sample, however, locating each indent is challenging and we used an averaged Young’s modulus for each sample, which means heterogeneous changes within a shale sample is ignored from the output end. In the further, we would like to link the variability of the microindentation data to the variability of the element maps for the next step.

## 5 Conclusion

In this study, a deep learning CNNs model was employed on 2D elemental intensity distribution maps to predict the mechanical properties of shales. The proposed CNNs model framework followed: (a) collecting element intensity maps for nine major elements abundant in a shale, including Al, Ca, C, Fe, K, Mg, Na, S, and Si; (b) mechanical properties’ collection, Young’s modulus of the corresponding samples; (c) CNNs model building, and training based on the images and mechanical properties datasets, and (d) mechanical properties prediction using the trained CNNs model. The input data were created from SEM–EDS mapping, and the ground truth data were Young’s modulus values corresponding to each image obtained from microindentation tests. A total of 800 images obtained from ten shale samples were used for training and testing. The results showed that the predicted Young’s modulus values had an averaged relative error of 6.5%, which is in an acceptable error range compared to the laboratory errors. In addition, the prediction of the mechanical parameters of rocks by this newly proposed method can be an alternative to the laboratory approaches where sample preparation and more elaborate data interpretation would be inevitable.

**Author contributions** CL: methodology, coding, data analysis, and draft manuscript. DW: supervise and editing. LK: data analysis and making figures. MO: editing.

**Funding** No found for this study.

### Declarations

**Conflict of interest** The authors declare that they have no known competing financial interests or personal relationships that could have appeared to influence the work reported in this paper.

**Data availability** The data and material can be available for reader’s request.

**Code availability** Code can be available as requested.

## References

- Abarghani A, Ostadhassan M, Gentzis T, Carvajal-Ortiz H, Bubach B (2018) Organofacies study of the Bakken source rock in North Dakota, USA, based on organic petrology and geochemistry. *Int J Coal Geol* 188:79–93. <https://doi.org/10.1016/j.coal.2018.02.004>
- Abarghani A, Ostadhassan M, Bubach B, Zhao P (2019) Estimation of thermal maturity in the Bakken source rock from a combination of well logs, North Dakota, USA. *Mar Pet Geol* 105:32–44. <https://doi.org/10.1016/j.marpetgeo.2019.04.005>
- Abedi S, Slim M, Hofmann R, Bryndzia T, Ulm F-J (2016a) Nanochemo-mechanical signature of organic-rich shales: a coupled indentation–EDX analysis. *Acta Geotech* 11:559–572. <https://doi.org/10.1007/s11440-015-0426-4>
- Abedi S, Slim M, Ulm F-J (2016b) Nanomechanics of organic-rich shales: the role of thermal maturity and organic matter content on texture. *Acta Geotech* 11:775–787
- Bobko CP (2008) Assessing the mechanical microstructure of shale by nanoindentation: the link between mineral composition and mechanical properties. Massachusetts Institute of Technology, Massachusetts
- Bobko C, Ulm F-J (2008) The nano-mechanical morphology of shale. *Mech Mater* 40:318–337
- Constantinides G, Chandran KR, Ulm F-J, Van Vliet K (2006) Grid indentation analysis of composite microstructure and mechanics: principles and validation. *Mater Sci Eng A* 430:189–202
- Dahi-Taleghani A, Olson JE et al (2011) Numerical modeling of multi-stranded-hydraulic-fracture propagation: accounting for the interaction between induced and natural fractures. *SPE J* 16:575–581
- Fischer-Cripps AC (2011) Nanoindentation. Mechanical engineering series, 3rd edn. Springer, New York
- Goodarzi M, Rouainia M, Aplin AC (2016) Numerical evaluation of mean-field homogenisation methods for predicting shale elastic response. *Comput Geosci* 20:1109–1122. <https://doi.org/10.1007/s10596-016-9579-y>
- Goodarzi M, Rouainia M, Aplin AC, Cubillas P, de Block M (2017) Predicting the elastic response of organic-rich shale using nanoscale measurements and homogenisation methods: predicting the response of organic-rich shale. *Geophys Prospect* 65:1597–1614. <https://doi.org/10.1111/1365-2478.12475>
- Goodfellow I, Bengio Y, Courville A (2016) Deep learning. MIT press, Cambridge
- Gupta I, Devegowda D, Jayaram V, Rai C, Sondergeld C (2019) Machine learning regressors and their metrics to predict synthetic sonic and mechanical properties 56
- Hassoun MH et al (1995) Fundamentals of artificial neural networks. MIT press, Cambridge
- He K, Zhang X, Ren S, Sun J (2016) Deep residual learning for image recognition. In: 2016 IEEE conference on computer vision and pattern recognition (CVPR). Presented at the 2016 IEEE conference on computer vision and pattern recognition (CVPR), IEEE, Las Vegas, NV, USA, pp. 770–778. Doi: <https://doi.org/10.1109/CVPR.2016.90>
- He J, Misra S, Li H (2018) Comparative study of shallow learning models for generating compressional and shear traveltime logs. *Petrophysics* 59:826–840
- Hertz H (1881) On the contact of elastic solids. *Z Reine Angew Math* 92:156–171
- Hoek E, Martin CD (2014) Fracture initiation and propagation in intact rock—a review. *J Rock Mech Geotech Eng* 6:287–300. <https://doi.org/10.1016/j.jrmge.2014.06.001>
- Hu C, Li Z (2015) A review on the mechanical properties of cement-based materials measured by nanoindentation. *Constr Build Mater* 90:80–90. <https://doi.org/10.1016/j.conbuildmat.2015.05.008>
- Izadi H, Sadri J, Mehran N-A (2015) A new intelligent method for minerals segmentation in thin sections based on a novel incremental color clustering. *Comput Geosci* 81:38–52. <https://doi.org/10.1016/j.cageo.2015.04.008>
- Khan MR, Tariq Z, Abdulraheem A (2018) Machine learning derived correlation to determine water saturation in complex lithologies. Presented at the SPE Kingdom of Saudi Arabia annual technical symposium and exhibition, Society of Petroleum Engineers. Doi: <https://doi.org/10.2118/192307-MS>
- Knaup A, Jernigen J, Curtis M, Sholeen J, Borer JJ, Sondergeld C, Rai C (2019) Unconventional reservoir microstructural analysis using SEM and machine learning. Presented at the SPE/AAPG/SEG unconventional resources technology conference, unconventional resources technology conference. Doi: <https://doi.org/10.5530/urtec-2019-638>
- Krizhevsky A, Sutskever I, Hinton GE (2012) ImageNet classification with deep convolutional neural networks. In: Pereira F, Burges CJC, Bottou L, Weinberger KQ (eds) *Advances in neural information processing systems*, vol 25. Curran Associates Inc, New York, pp 1097–1105
- Laws N (1977) The determination of stress and strain concentrations at an ellipsoidal inclusion in an anisotropic material. *J Elast* 7:91–97. <https://doi.org/10.1007/BF00041133>
- Li C, Ostadhassan M, Gentzis T, Kong L, Carvajal-Ortiz H, Bubach B (2018a) Nanomechanical characterization of organic matter in the Bakken formation by microscopy-based method. *Mar Pet Geol* 96:128–138. <https://doi.org/10.1016/j.marpetgeo.2018.05.019>
- Li C, Ostadhassan M, Guo S, Gentzis T, Kong L (2018b) Application of PeakForce tapping mode of atomic force microscope to characterize nanomechanical properties of organic matter of the Bakken Shale. *Fuel* 233:894–910. <https://doi.org/10.1016/j.fuel.2018.06.021>
- Li C, Ostadhassan M, Abarghani A, Fogden A, Kong L (2019a) Multi-scale evaluation of mechanical properties of the Bakken shale. *J Mater Sci* 54:2133–2151. <https://doi.org/10.1007/s10853-018-2946-4>
- Li C, Ostadhassan M, Kong L, Bubach B (2019b) Multi-scale assessment of mechanical properties of organic-rich shales: a coupled nanoindentation, deconvolution analysis, and homogenization method. *J Pet Sci Eng* 174:80–91. <https://doi.org/10.1016/j.petrol.2018.10.106>
- Li X, Liu Z, Cui S, Luo C, Li C, Zhuang Z (2019c) Predicting the effective mechanical property of heterogeneous materials by image based modeling and deep learning. *Comput Methods Appl Mech Eng* 347:735–753. <https://doi.org/10.1016/j.cma.2019.01.005>
- Li C, Wang D, Kong L (2021a) Mechanical response of the Middle Bakken rocks under triaxial compressive test and nanoindentation. *Int J Rock Mech Min Sci* 139:104660. <https://doi.org/10.1016/j.ijrmms.2021.104660>
- Li C, Wang D, Kong L (2021b) Application of machine learning techniques in mineral classification for scanning electron microscopy—energy dispersive X-ray spectroscopy (SEM-EDS) images. *J Pet Sci Eng* 200:108178. <https://doi.org/10.1016/j.petrol.2020.108178>
- Liu K, Ostadhassan M, Bubach B, Ling K, Tokhmechi B, Robert D (2018) Statistical grid nanoindentation analysis to estimate macro-mechanical properties of the Bakken Shale. *J Nat Gas Sci Eng* 53:181–190. <https://doi.org/10.1016/j.jngse.2018.03.005>
- Misra S, Li H, He J (2019) Machine learning for subsurface characterization. Gulf Professional Publishing, Houston
- Mori T, Tanaka K (1973) Average stress in matrix and average elastic energy of materials with misfitting inclusions. *Acta Metall* 21:571–574

- Oliver WC, Pharr GM (1992) An improved technique for determining hardness and elastic modulus using load and displacement sensing indentation experiments. *J Mater Res* 7:1564–1583
- Oliver WC, Pharr GM (2004) Measurement of hardness and elastic modulus by instrumented indentation: advances in understanding and refinements to methodology. *J Mater Res* 19:3–20. <https://doi.org/10.1557/jmr.2004.19.1.3>
- Saif T, Lin Q, Butcher AR, Bijeljic B, Blunt MJ (2017) Multi-scale multi-dimensional microstructure imaging of oil shale pyrolysis using X-ray micro-tomography, automated ultra-high resolution SEM, MAPS Mineralogy and FIB-SEM. *Appl Energy* 202:628–647. <https://doi.org/10.1016/j.apenergy.2017.05.039>
- Saraji S, Piri M (2015) The representative sample size in shale oil rocks and nano-scale characterization of transport properties. *Int J Coal Geol* 146:42–54. <https://doi.org/10.1016/j.coal.2015.04.005>
- Sayers CM (2013) The effect of anisotropy on the Young's moduli and Poisson's ratios of shales: the effect of anisotropy on the Young's moduli and Poisson's ratios of shales. *Geophys Prospect* 61:416–426. <https://doi.org/10.1111/j.1365-2478.2012.01130.x>
- Shindo D, Oikawa T (2002) Energy dispersive X-ray spectroscopy. In: Shindo D, Oikawa T (eds) *Analytical electron microscopy for materials science*. Springer, Tokyo, pp 81–102. [https://doi.org/10.1007/978-4-431-66988-3\\_4](https://doi.org/10.1007/978-4-431-66988-3_4)
- Simard PY, Steinkraus D, Platt JC (2003) J.C.: Best practices for convolutional neural networks applied to visual document analysis. In: *Int'l conference on document analysis and recognition*. pp. 958–963
- Simonyan K, Zisserman A (2015) Very deep convolutional networks for large-scale image recognition. *ArXiv14091556 Cs*
- Sultana F, Sufian A, Dutta P (2018) Advancements in image classification using convolutional neural network. In: *2018 Fourth international conference on research in computational intelligence and communication networks (ICRCICN)*. Presented at the 2018 fourth international conference on research in computational intelligence and communication networks (ICRCICN), pp. 122–129. Doi: <https://doi.org/10.1109/ICRCICN.2018.8718718>
- Szegedy C, Wei L, Yangqing J, Sermanet P, Reed S, Anguelov D, Erhan D, Vanhoucke V, Rabinovich A (2015) Going deeper with convolutions. In: *2015 IEEE conference on computer vision and pattern recognition (CVPR)*. Presented at the 2015 IEEE conference on computer vision and pattern recognition (CVPR), IEEE, Boston, MA, USA, pp. 1–9. Doi: <https://doi.org/10.1109/CVPR.2015.7298594>
- Tang D, Spikes K (2017) Segmentation of shale SEM images using machine learning. In: *SEG technical program expanded abstracts 2017*. Presented at the SEG technical program expanded abstracts 2017, society of exploration geophysicists, Houston, Texas, pp. 3898–3902. Doi: <https://doi.org/10.1190/segam2017-17738502.1>
- Torlov V, Bonavides C, Belowi A (2017) Data driven assessment of rotary sidewall coring performance. In: *SPE annual technical conference and exhibition*. Presented at the SPE annual technical conference and exhibition, society of petroleum engineers, San Antonio, Texas, USA. Doi: <https://doi.org/10.2118/187107-MS>
- Ulm F-J, Aboalsleiman Y (2006) The nanogranular nature of shale. *Acta Geotech* 1:77–88
- Veytskin YB, Tammina VK, Bobko CP, Hartley PG, Clennell MB, Dewhurst DN, Dagastine RR (2017) Micromechanical characterization of shales through nanoindentation and energy dispersive x-ray spectrometry. *Geomech Energy Environ* 9:21–35
- Wenner S, Jones L, Marioara CD, Holmestad R (2017) Atomic-resolution chemical mapping of ordered precipitates in Al alloys using energy-dispersive X-ray spectroscopy. *Micron* 96:103–111. <https://doi.org/10.1016/j.micron.2017.02.007>
- Zhao J, Zhang D, Wu T, Tang H, Xuan Q, Jiang Z, Dai C (2019) Multiscale approach for mechanical characterization of organic-rich shale and its application. *Int J Geomech* 19:04018180. [https://doi.org/10.1061/\(ASCE\)GM.1943-5622.0001281](https://doi.org/10.1061/(ASCE)GM.1943-5622.0001281)

**Publisher's Note** Springer Nature remains neutral with regard to jurisdictional claims in published maps and institutional affiliations.